

On-the-fly training of polynomial machine learning potentials in computing lattice thermal conductivity

Atsushi Togo^{1,*} and Atsuto Seko²

¹*Center for Basic Research on Materials National Institute for Materials Science, Tsukuba, Ibaraki 305-0047, Japan*

²*Department of Materials Science and Engineering,
Kyoto University, Sakyo, Kyoto 606-8501, Japan*

The application of first-principles calculations for predicting lattice thermal conductivity (LTC) in crystalline materials, in conjunction with the linearized phonon Boltzmann equation, has gained increasing popularity. In this calculation, the determination of force constants through first-principles calculations is critical for accurate LTC predictions. For material exploration, performing first-principles LTC calculations in a high-throughput manner is now expected, although it requires significant computational resources. To reduce computational demands, we integrated polynomial machine learning potentials on-the-fly during the first-principles LTC calculations. This paper presents a systematic approach to first-principles LTC calculations. We designed and optimized an efficient workflow that integrates multiple modular software packages. We applied this approach to calculate LTCs for 103 compounds of the wurtzite, zincblende, and rocksalt types to evaluate the performance of the polynomial machine learning potentials in LTC calculations. We demonstrate a significant reduction in the computational resources required for the LTC predictions.

I. INTRODUCTION

Calculations of lattice thermal conductivity (LTC) based on first-principles calculations and the linearized phonon Boltzmann equation [1–4] have become increasingly popular in recent years. This is because sufficiently accurate LTC values can be systematically predicted for a wide variety of crystals using available computer simulation packages.[5–10] These computational tools are expected to be applied in materials discovery within a high-throughput calculation environment. However, since first-principles LTC calculations are still computationally intensive, there is a need for the development of methodologies to reduce the computational demands.

We conventionally employ a supercell approach combined with the finite displacement method for first-principles LTC calculations. Random or systematic displacements are introduced to the supercells, and the forces on atoms are calculated using first-principles calculations. Subsequently, supercell force constants are computed from the dataset composed of the displacements and forces, and the LTC values are calculated from these supercell force constants. Many supercells with different displacement configurations are often required to populate the tensor elements of the supercell force constants.

The accuracy of predicting LTCs relies on the use of first-principles calculations to obtain the displacement-force dataset. However, this approach is computationally intensive. In order to achieve precise LTC predictions with lower computational resources, compressive sensing force constants calculation methods were developed, as reported in Refs. 11 and 12. These methods employ regularized linear regression techniques to eliminate certain tensor elements of the supercell force constants,

thereby reducing the required size of the displacement-force dataset.

In this study, we introduce another approach to reduce the computational demands of first-principles LTC calculations. We incorporate polynomial machine learning potentials (MLPs) [13, 14] into an intermediate stage of the LTC calculation process. The polynomial MLPs are trained using a small dataset of displacement-force pairs and energies derived from first-principles calculations. Subsequently, the polynomial MLPs generate a large displacement-force dataset to calculate supercell force constants with significantly lower computational demands than those required by first-principles calculations. Compared to the compressive sensing approach, this approach may more efficiently represent energy surface of crystal potential. However, the workflow for performing the first-principles LTC calculation with this approach is more complex. One objective of this study is to encapsulate this intricate workflow into a software package, complete with a set of well-optimized default parameters. Developing this software package requires a thorough understanding of the MLP code details. Moreover, efficient estimations of polynomial MLPs can be accomplished using linear regressions supported by powerful libraries for linear algebra. Therefore, we have utilized the polynomial MLP code developed by one of the authors.

The computational procedure is illustrated in Fig. 1. Initially, a set of supercells with random displacements of atoms is prepared. Forces on atoms and energies in the supercells are calculated using first-principles calculations. The dataset, consisting of displacement-force pairs and energies, is employed to train the polynomial MLPs. Forces on atoms in another set of supercells with random displacements of atoms are calculated using the trained polynomial MLPs. Supercell force constants are then calculated from the displacement-force dataset obtained through the polynomial MLPs. Finally, the LTC

* Author to whom any correspondence should be addressed. togo.atsushi@nims.go.jp

values are calculated using the supercell force constants obtained. Crystal symmetry plays an important role in reducing the computational demands and improving the numerical accuracy.

The goal of the methodological and software developments presented in this study is to reduce the computational demands of first-principles LTC calculations, with the aim of high-throughput LTC calculations. At the same time, we prioritize user convenience, considering factors such as calculation time and required memory. We have designed the workflow and software to make the use of the polynomial MLPs appear straightforward from the user’s perspective. This study explores the feasibility of employing polynomial MLPs as an intermediate stage in the calculation of third-order supercell force constants for first-principles LTC calculations.

In this study, a systematic calculation of LTCs at 300 K was performed for the same set of the 103 compounds of wurtzite, zincblende, and rocksalt types reported in Ref. 15. The computational workflow-design and details are presented in Secs. II and III. While most of the theoretical and methodological background is covered in the referenced articles, those relevant to this paper are described in Sec. III. The results of the LTC calculations are summarized in Sec. IV.

II. DESIGN OF COMPUTATIONAL WORKFLOW

As shown in Fig. 1, our study utilized a specific approach for LTC calculations. This approach consists of specialized modules for each calculation step. These modules are interconnected through a local file system and data communication, including computer-network file transfers and application program interfaces (APIs).

In the LTC calculation process, we generate two distinct sets of supercells with random displacements of atoms. This occurs in steps (a) and (d), as illustrated in Fig. 1. In this study, we displaced atoms by a constant distance in random directions. In step (b), we conduct energy and force calculations for the first set of supercells using first-principles calculations. This is the most computationally demanding step. The outputs of step (b) form a dataset used to train polynomial MLPs in step (c). In step (e), we calculate forces for the second set of supercells using the trained polynomial MLPs. In step (f), third-order supercell force constants are computed using the displacement-force dataset from step (e). Finally in step (g), LTC is calculated from the supercell force constants. Use of crystal symmetry is important in steps (f) and (g) for the computational efficiency and numerical accuracy. The computational demand from step (c) to the end is negligible compared to step (b).

Our computational workflow is specifically designed to optimize high-throughput LTC calculations, balancing efficiency and convenience. This workflow is divided into two main parts: dataset preparation and calculations us-

ing this dataset. The dataset preparation stage involves a set of energy and force calculations using first-principles calculations, which are normally distributed over computer nodes to conduct the calculations in parallel. After completing these calculations, we extract the necessary data from the output files of the first-principles calculations. This data is then saved for transfer via computer-network communication. In the subsequent steps, calculations are performed on a single computer. Depending on the operational requirements, data transfer between the modules is facilitated either through APIs or via the local computer file system for ease of use.

III. COMPUTATIONAL METHODS

A. LTC calculation

LTC values were computed by solving the Peierls-Boltzmann equation within the relaxation time approximation (RTA)[1, 2, 16] using the phono3py code.[9, 17] It is important to note that the method employed for the LTC calculations may not be appropriate for compounds with low or high thermal conductivity among the 103 compounds selected. To simplify the methodological investigation in this study, we considered only phonon-phonon scattering for determining the phonon relaxation times. Imaginary parts of phonon self-energies corresponding to the bubble diagram were calculated from supercell force constants, where a linear tetrahedron method was used to treat the delta function,[17] and their reciprocals were used as the relaxation times. Computational details on the calculation of the supercell force constants are provided in the subsequent sections. Phonon group velocities, mode heat capacities, frequencies, and eigenvectors were obtained from dynamical matrices constructed using second-order supercell force constants. Additionally, a non-analytical term correction [18–20] was applied to the dynamical matrices to account for long-range dipole-dipole interactions in the harmonic phonon calculation. For the wurtzite-type compounds, reciprocal spaces were sampled using a $19 \times 19 \times 10$ mesh, while a $19 \times 19 \times 19$ mesh was employed for the zincblende-type and rocksalt-type compounds.

B. Supercell force constants calculation

Force constants required for predicting LTCs are determined as the coefficients $\Phi_{l\nu\alpha,\dots}$ in the Taylor expansion of the potential energy \mathcal{V} with respect to atomic

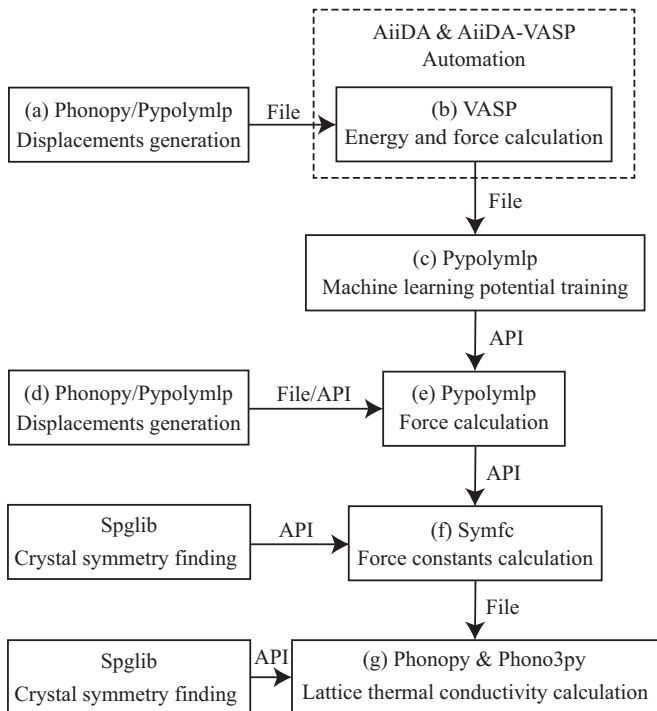


FIG. 1. Schematic illustration of workflow employed in this study for LTC calculations. Each calculation step is represented by a box, within which the name of the software package and the type of calculation are described. The arrows roughly indicate flow of data. The data were passed via APIs or computer files. The steps are as follows: Step (a): Generation of a modest number of supercells with random displacements. Step (b): Calculation of energies and forces in the supercells generated in step (a) by first-principles calculations. The submission of a large number of computational jobs is automated using a workflow system. Step (c): Training of polynomial MLPs using the energies and forces in the supercells obtained in step (b). Step (d): Generation of a large number of supercells with random displacements. Step (e): Calculation of forces in the supercells generated in step (d) using the trained polynomial MLPs. Step (f): Calculation of force constants from the displacement-force dataset calculated in step (e). Step (g): Calculation of LTC using the supercell force constants obtained in step (f). This study introduces steps (c), (d), and (e) to the workflow. Conventionally, the dataset from step (b) is used directly in step (f). This conventional approach is computationally demanding due to the necessity of a large dataset in step (b). In this workflow, second-order force constants can be calculated in the conventional approach because the computational demand is much less than the calculation of third-order force constants in the conventional approach.

displacements $u_{l\kappa\alpha}$:

$$\begin{aligned} \mathcal{V} = & \Phi_0 + \sum_{l\kappa\alpha} \Phi_{l\kappa\alpha} u_{l\kappa\alpha} \\ & + \frac{1}{2} \sum_{l\kappa\alpha, l'\kappa'\alpha'} \Phi_{l\kappa\alpha, l'\kappa'\alpha'} u_{l\kappa\alpha} u_{l'\kappa'\alpha'} \\ & + \frac{1}{3!} \sum_{l\kappa\alpha, l'\kappa'\alpha', l''\kappa''\alpha''} \Phi_{l\kappa\alpha, l'\kappa'\alpha', l''\kappa''\alpha''} u_{l\kappa\alpha} u_{l'\kappa'\alpha'} u_{l''\kappa''\alpha''} + \dots, \end{aligned} \quad (1)$$

where l , κ , and α represent the unit cell, atom index within the unit cell, and Cartesian coordinate, respectively. By differentiating both sides of Eq. (1) with respect to $u_{l\kappa\alpha}$, we obtain

$$\begin{aligned} -f_{l\kappa\alpha} = & \Phi_{l\kappa\alpha} + \sum_{l'\kappa'\alpha'} \Phi_{l\kappa\alpha, l'\kappa'\alpha'} u_{l'\kappa'\alpha'} \\ & + \frac{1}{2} \sum_{l'\kappa'\alpha', l''\kappa''\alpha''} \Phi_{l\kappa\alpha, l'\kappa'\alpha', l''\kappa''\alpha''} u_{l'\kappa'\alpha'} u_{l''\kappa''\alpha''} \\ & + \dots, \end{aligned} \quad (2)$$

where $f_{l\kappa\alpha}$ represents the α -component of the force on atom $l\kappa$. In this study, we obtain these coefficients by fitting a dataset consisting of finite displacements and forces of atoms in supercells approximating Eq. (2). The equation that we employ for fitting the third-order supercell force constants is written as

$$\begin{aligned} -F_{l\kappa\alpha} = & \sum_{l'\kappa'\alpha'} \Phi_{l\kappa\alpha, l'\kappa'\alpha'}^{\text{SC}} U_{l'\kappa'\alpha'} \\ & + \frac{1}{2} \sum_{l'\kappa'\alpha', l''\kappa''\alpha''} \Phi_{l\kappa\alpha, l'\kappa'\alpha', l''\kappa''\alpha''}^{\text{SC}} U_{l'\kappa'\alpha'} U_{l''\kappa''\alpha''}, \end{aligned} \quad (3)$$

where $F_{l\kappa\alpha}$ and $U_{l\kappa\alpha}$ represent the forces and displacements of atoms in supercells, respectively. $\Phi_{l\kappa\alpha, l'\kappa'\alpha'}^{\text{SC}}$ and $\Phi_{l\kappa\alpha, l'\kappa'\alpha', l''\kappa''\alpha''}^{\text{SC}}$ denote the second- and third-order supercell force constants, respectively. Here we assume $\Phi_{l\kappa\alpha}^{\text{SC}} = 0$.

Higher-order terms are effectively included in $\Phi_{l\kappa\alpha, l'\kappa'\alpha'}^{\text{SC}}$ and $\Phi_{l\kappa\alpha, l'\kappa'\alpha', l''\kappa''\alpha''}^{\text{SC}}$. In Eq. (3), the contributions from higher-order terms are expected to become negligible as the displacements become smaller. However, use of smaller displacements can make the computation of supercell force constants more susceptible to numerical errors of forces. To find a compromise between these conflicting requirements, a modest inclusion of higher-order contributions is commonly adopted. Higher-order terms also introduce additional degrees of freedom. To average over them in the third-order supercell force constants, a larger displacement-force dataset is required to achieve convergence in LTC values.

The linear regression method was employed to calculate supercell force constants from the displacement-force dataset. In this method, forces acting on atoms, which were randomly displaced from their equilibrium positions

in supercells, were computed either using the polynomial MLPs in our current approach or through first-principles calculations in the conventional approach. Tensor elements of supercell force constants were projected onto the subspace defined by symmetry projection operators of totally symmetric irreducible representations of the space group, index permutation, and translational invariance. In addition, detailed techniques were developed to enhance the efficiency of this computational process. This process is implemented in the symfc code.[21, 22] The crystallographic symmetries were determined using the spglib code.[23]

For the zincblende- and rocksalt-type compounds, we utilized supercells with $2 \times 2 \times 2$ and $4 \times 4 \times 4$ expansions of the conventional unit cells to calculate third-order and second-order supercell force constants, respectively. In the case of the wurtzite-type compounds, supercells with $3 \times 3 \times 2$ and $5 \times 5 \times 3$ expansions of the unit cells were employed for third-order and second-order supercell force constants calculations, respectively.

To compute the second-order supercell force constants, we employed the finite difference method as implemented in the phonopy code.[15, 17] We used the same displacement-force datasets as those in Ref. 15, where the forces in these datasets had been computed through first-principles calculations. The number of supercells in the datasets were six, two, and two for the wurtzite-, zincblende-, and rocksalt-type compounds, respectively.

Third-order supercell force constants were calculated from the displacement-force datasets using the symfc code.[21] The numbers of symmetrically independent force constant elements were 7752, 1536, and 758 for the wurtzite-, zincblende-, and rocksalt-type compounds, respectively. These values were determined based on the forces acting on atoms, which were inferred using the polynomial MLPs implemented in the pypolympl code.[14]

C. Polynomial MLPs

The polynomial MLPs were trained using the dataset composed of forces and displacements of atoms and energies in supercells. These energies and forces were computed through first-principles calculations. The performance of the polynomial MLPs in the LTC calculation via the third-order supercell force constants is discussed in Section IV.

For the 103 compounds, we trained the polynomial MLPs using the pypolympl code.[14] In this training, Gaussian-type radial functions were employed, and the functional form $f_n(r)$ is given as

$$f_n(r) = \exp[-\beta_n(r - r_n)^2] f_c(r), \quad (4)$$

$$f_c(r) = \begin{cases} [\cos(\pi r/r_c) + 1]/2 & (r \leq r_c), \\ 0 & (r > r_c). \end{cases} \quad (5)$$

where r represents the distance from the center of each

atom, and r_c is the cutoff distance. β_n and r_n are the parameters, respectively. Radial functions with $r_c = 8.0$ Å and $\beta_n = 1.0$ Å⁻² and $r_n = (n - 1)(r_c - 1.0)/11$ for $n = 1, \dots, 12$ were used. We considered polynomial invariants up to third order characterizing neighboring atomic density based on spherical harmonics with the maximum angular numbers of spherical harmonics $l_{\max}^{(2)} = l_{\max}^{(3)} = 8$. The polynomial models were then constructed by the polynomial functions of the pair invariants and linear polynomial function of the polynomial invariants. We considered polynomial functions up to second order. The model coefficients were estimated from electronic total energies and forces by the linear ridge regression method.

D. First-principles calculation

For the first-principles calculations, we employed the plane-wave basis projector augmented wave (PAW) method [24] within the framework of DFT as implemented in the VASP code.[25–27] The generalized gradient approximation (GGA) of Perdew, Burke, and Ernzerhof revised for solids (PBEsol) [28] was used as the exchange correlation potential. To ensure high numerical accuracy in computing atomic forces, the projection operators were applied in reciprocal spaces and additional support grids were employed for the evaluation of the augmentation charges. Static dielectric constants and Born effective charges were calculated with the conventional unit cells from density functional perturbation theory (DFPT) as implemented in the VASP code.[29, 30]

A plane-wave energy cutoff of 520 eV was employed for the supercell force calculations and 676 eV for the DFPT calculations. Reciprocal spaces of the zincblende- and rocksalt-type compounds were sampled by the half-shifted $2 \times 2 \times 2$ meshes for the $2 \times 2 \times 2$ supercells, the half-shifted $1 \times 1 \times 1$ meshes for the $4 \times 4 \times 4$ supercells, and the half-shifted $8 \times 8 \times 8$ meshes for the conventional unit cells. Reciprocal spaces of the wurtzite-type compounds were sampled by the $2 \times 2 \times 2$ meshes that are half-shifted along the c^* axis for the $3 \times 3 \times 2$ supercells, the $1 \times 1 \times 2$ meshes that are half-shifted along the c^* axis for the $5 \times 5 \times 3$ supercells, and the $12 \times 12 \times 8$ meshes that are half-shifted along the c^* axis for the unit cells.

E. Automation of dataset preparation

Performing a large number of first-principles calculations can be computationally intensive and may require high-performance computing resources. This stage consumes a significant amount of computational power throughout the LTC calculation process. It is virtually inevitable that some of these calculations fail for various reasons, such as reaching the maximum number of electronic structure convergence iterations or encountering issues related to computer networks and hardware.

Although the proportion of failed calculations was relatively low, we have not yet fully automated error recovery for all possible cases.

We systematically identified calculation failures and re-executed those calculations semi-manually with the assistance of the workflow system instead of attempting to fully automate all processes. After completing all the supercell calculations using first-principles calculations, the dataset for each compound required for the subsequent LTC calculation process was composed into a single computer file in a structured format.

For the systematic calculations of energies and forces in supercells using first-principles calculations, we utilized the AiiDA environment [31–33] in conjunction with the AiiDA-VASP plugin.[34] The advantage of using the workflow automation system was not only the automation of submitting calculation jobs to high-performance computers, but also the automated data storing of the calculation results in a database systematically. The computed data, stored within the AiiDA database, could be conveniently accessed through the Python programming language. By writing a concise Python script, we were able to extract supercell energies, forces, and displacements from the AiiDA database on demand and convert this data into the structured format required for immediate use by the phono3py code.[9, 17] An example of the phono3py data format can be found in the phono3py github repository.

F. Parameters for 103 binary compounds

33 compounds for the wurtzite- and zincblende-type and 37 compounds for the rocksalt-type were used to evaluate the LCT calculation approach proposed in this study, and their chemical compositions are listed in Tables I and II. Crystal structures of the wurtzite and zincblende types are similar, though their stacking orders are different, much like the relationship between face-centered-cubic and hexagonal-close-packed structure types. Since it is of interest to explore their similarities and differences in calculations, as also studied in Ref. 9, the compounds with the same chemical compositions for the wurtzite and zincblende types were calculated. The tables also provide information on lattice parameters, the choices of PAW datasets from the VASP package, and electronic total energies of the elements that were subtracted from the total energies of the compounds used to train the polynomial MLPs.

IV. RESULTS

A. Choice of displacements and number of supercells

For each compound, two distinct displacement-force datasets that share the same supercell basis vectors were

TABLE I. Lattice parameters, names of the VASP PAW-PBE datasets, electronic total energies of the atoms used in this study for 33 wurtzite- and zincblende-type compounds. w - a , w - c , and z - a denote the lattice parameters a and c of the wurtzite-type compounds, and a of the zincblende-type compounds, respectively.

	w - a	w - c	z - a		energy (eV)		energy (eV)
AgI	4.56	7.45	6.44	(Ag_pv)	-0.233	(I)	-0.182
AlAs	4.00	6.58	5.67	(Al)	-0.282	(As_d)	-0.989
AlN	3.11	4.98	4.38	(Al)	-0.282	(N)	-1.905
AlP	3.86	6.34	5.47	(Al)	-0.282	(P)	-1.140
AlSb	4.35	7.16	6.17	(Al)	-0.282	(Sb)	-0.828
BAAs	3.35	5.55	4.77	(B)	-0.359	(As_d)	-0.989
BeO	2.70	4.38	3.80	(Be)	-0.023	(O)	-0.957
BeS	3.41	5.63	4.84	(Be)	-0.023	(S)	-0.578
BeSe	3.62	5.97	5.14	(Be)	-0.023	(Se)	-0.438
BeTe	3.95	6.53	5.61	(Be)	-0.023	(Te)	-0.359
BN	2.54	4.20	3.61	(B)	-0.359	(N)	-1.905
BP	3.18	5.27	4.52	(B)	-0.359	(P)	-1.140
CdS	4.13	6.72	5.84	(Cd)	-0.021	(S)	-0.578
CdSe	4.31	7.03	6.09	(Cd)	-0.021	(Se)	-0.438
CdTe	4.59	7.52	6.50	(Cd)	-0.021	(Te)	-0.359
CuBr	3.92	6.48	5.56	(Cu_pv)	-0.274	(Br)	-0.225
CuCl	3.70	6.17	5.27	(Cu_pv)	-0.274	(Cl)	-0.311
CuH	2.81	4.44	3.93	(Cu_pv)	-0.274	(H)	-0.946
CuI	4.17	6.88	5.92	(Cu_pv)	-0.274	(I)	-0.182
GaAs	3.99	6.57	5.66	(Ga_d)	-0.286	(As_d)	-0.989
GaN	3.18	5.18	4.50	(Ga_d)	-0.286	(N)	-1.905
GaP	3.83	6.31	5.44	(Ga_d)	-0.286	(P)	-1.140
GaSb	4.31	7.10	6.11	(Ga_d)	-0.286	(Sb)	-0.828
InAs	4.30	7.05	6.09	(In_d)	-0.264	(As_d)	-0.989
InN	3.54	5.71	4.99	(In_d)	-0.264	(N)	-1.905
InP	4.15	6.81	5.88	(In_d)	-0.264	(P)	-1.140
InSb	4.60	7.56	6.52	(In_d)	-0.264	(Sb)	-0.828
MgTe	4.56	7.41	6.44	(Mg_pv)	-0.009	(Te)	-0.359
SiC	3.08	5.05	4.36	(Si)	-0.522	(C)	-1.340
ZnO	3.24	5.23	4.56	(Zn)	-0.016	(O)	-0.957
ZnS	3.79	6.21	5.36	(Zn)	-0.016	(S)	-0.578
ZnSe	3.98	6.54	5.64	(Zn)	-0.016	(Se)	-0.438
ZnTe	4.28	7.05	6.07	(Zn)	-0.016	(Te)	-0.359

employed to calculate LTCs. Energies and forces of the supercells in the first dataset were computed using first-principles calculations, while the polynomial MLPs were utilized for calculating forces in the second dataset. The first dataset was used to train the polynomial MLPs. The second dataset was employed to compute third-order supercell force constants by fitting.

To investigate the performance of the polynomial MLPs in predicting LTC values, 100 supercells with random directional displacements were initially prepared as the first dataset. Subsequently, the first 10, 20, 40, 60,

TABLE II. Lattice parameters a , names of the VASP PAW-PBE datasets, and electronic total energies of the atoms used in this study for 37 rocksalt-type compounds.

	a	energy (eV)	energy (eV)		energy (eV)
AgBr	5.67	(Ag_pv)	-0.233	(Br)	-0.225
AgCl	5.44	(Ag_pv)	-0.233	(Cl)	-0.311
BaO	5.53	(Ba_sv)	-0.035	(O)	-0.957
BaS	6.36	(Ba_sv)	-0.035	(S)	-0.578
BaSe	6.58	(Ba_sv)	-0.035	(Se)	-0.438
BaTe	6.97	(Ba_sv)	-0.035	(Te)	-0.359
CaO	4.77	(Ca_pv)	-0.010	(O)	-0.957
CaS	5.63	(Ca_pv)	-0.010	(S)	-0.578
CaSe	5.87	(Ca_pv)	-0.010	(Se)	-0.438
CaTe	6.30	(Ca_pv)	-0.010	(Te)	-0.359
CdO	4.71	(Cd)	-0.021	(O)	-0.957
CsF	5.96	(Cs_sv)	-0.166	(F)	-0.556
KBr	6.59	(K_pv)	-0.182	(Br)	-0.225
KCl	6.29	(K_pv)	-0.182	(Cl)	-0.311
KF	5.37	(K_pv)	-0.182	(F)	-0.556
KH	5.63	(K_pv)	-0.182	(H)	-0.946
KI	7.05	(K_pv)	-0.182	(I)	-0.182
LiBr	5.41	(Li_sv)	-0.286	(Br)	-0.225
LiCl	5.06	(Li_sv)	-0.286	(Cl)	-0.311
LiF	4.00	(Li_sv)	-0.286	(F)	-0.556
LiH	3.97	(Li_sv)	-0.286	(H)	-0.946
LiI	5.90	(Li_sv)	-0.286	(I)	-0.182
MgO	4.22	(Mg_pv)	-0.009	(O)	-0.957
NaBr	5.93	(Na_pv)	-0.246	(Br)	-0.225
NaCl	5.60	(Na_pv)	-0.246	(Cl)	-0.311
NaF	4.63	(Na_pv)	-0.246	(F)	-0.556
NaH	4.79	(Na_pv)	-0.246	(H)	-0.946
NaI	6.41	(Na_pv)	-0.246	(I)	-0.182
PbS	5.90	(Pb_d)	-0.374	(S)	-0.578
PbSe	6.10	(Pb_d)	-0.374	(Se)	-0.438
PbTe	6.44	(Pb_d)	-0.374	(Te)	-0.359
RbBr	6.88	(Rb_pv)	-0.168	(Br)	-0.225
RbCl	6.58	(Rb_pv)	-0.168	(Cl)	-0.311
RbF	5.66	(Rb_pv)	-0.168	(F)	-0.556
RbH	5.95	(Rb_pv)	-0.168	(H)	-0.946
RbI	7.32	(Rb_pv)	-0.168	(I)	-0.182
SrO	5.13	(Sr_sv)	-0.032	(O)	-0.957

and 80 supercells were selected from the list of 100 supercells as subsets. Using the displacement-force pairs and energies of these supercells, the polynomial MLPs were trained, and the last 20 supercells were reserved as test data to optimize their ridge regularization parameters.

For the ease of use of the software package, we decided to employ a constant displacement distance, and to obtain reasonable LTC values, we chose a constant displacement distance of 0.03 Å. Interestingly, we found

that the polynomial MLPs performed well even with a relatively large displacement distance, such as 0.1 Å. It is important to note that these factors are highly dependent on the specific force calculators and calculation configurations used.

We utilized another displacement-force dataset that consists of 400 supercells with random directional displacements for the computation of third-order supercell force constants. These supercell forces were calculated using the trained polynomial MLPs, where the residual forces were subtracted. The root-mean-square errors of the polynomial MLPs trained on the 20 supercells ranged from approximately 5.5×10^{-6} to 1.4×10^{-3} eV/Å, which are expected to represent the same degree of numerical errors in the displacement-force dataset.

Due to the numerical smoothness of the polynomial MLPs for the force calculation with respect to positions of atoms compared to the first-principles calculations employed in this study, we were able to choose a small constant displacement distance of 0.001 Å. This benefits better convergence with smaller dataset when fitting the supercell force constants by Eq. (3). For instance, in the case of a displacement distance of 0.03 Å, it was necessary to employ 10000 supercells to achieve well converged LTC values for the 103 compounds. This suggests that when high-order force constants are more relevant for specific compounds, direct calculation of third-order supercell force constants from the displacement-force dataset through first-principles calculations may require a large dataset to achieve convergence of LTC values.

B. Calculated LTCs

In Figs. 2, 3, and 4, we present the calculated LTCs of the 103 compounds at 300 K. We can see that datasets with 20 supercells show good performance, at least for estimating LTC values roughly. In particular, the LTC values of most of the rocksalt-type compounds are well represented by these small datasets. The wurtzite- and zincblende-type compounds exhibit similar tendencies in LTC values with respect to dataset size since these crystal structures are similar. The datasets with 40 supercells yield LTC results that are roughly converged.

LTC values at 300 K predicted by the conventional approach, which directly uses the displacement-force dataset obtained through first-principles calculations to fit third-order supercell force constants, are depicted by the horizontal dotted lines. The third-order supercell force constants were computed by the linear regression method as implemented in the symfc code [21] from the first datasets with 100 supercells and 0.03 Å random directional displacements, which were those prepared for training the polynomial MLPs, as explained in Sec. IV A. In addition, LTC values with 400 supercells for the zincblende- and rocksalt-type compounds and those with 400 and 2000 supercells for the wurtzite-type compounds were also computed. These values are depicted

as horizontal lines in Figs. 2, 3, and 4. For most of the zincblende- and rocksalt-type compounds, LTC values derived from datasets with 100 supercells are found to be adequate when compared to those from 400 supercells. However, for the wurtzite-type compounds, even datasets with 400 supercells are insufficient.

The LTC values predicted for the wurtzite-type compounds using polynomial MLPs tend to align with those calculated directly from 2000 supercell datasets. This alignment emphasizes the utility and effectiveness of using polynomial MLPs in these cases.

C. Comparison with conventional LTC calculation

In Fig. 5, the LTC values of the 103 compounds calculated through the polynomial MLPs trained using the 20 supercell datasets are compared with those calculated in the conventional approach using the same finite-difference displacement-force datasets [35] as those employed in Ref. 15. These datasets share the same unit cells and supercell sizes for each compound. The latter datasets for the wurtzite-, zincblende-, and rocksalt-type compounds consist of 1254, 222, and 146 displacements, respectively, with a displacement distance of 0.03 Å. These displacements were systematically introduced considering crystal symmetries [36] by using the phono3py code.[9, 17] In all these calculations, the same version of the phono3py code [9, 17] (release v3.0.3) was utilized to calculate the LTCs from the respective supercell force constants. The results demonstrate that the LTC values obtained through the polynomial MLPs consistently agree with those predicted by the conventional approach.[15] The LTC values of the 103 compounds are also tabulated in Tables III and IV.

D. Conclusion

To improve the efficiency of high-throughput LTC calculations, we developed methodologies and modular software packages that utilize polynomial MLPs for computing LTC values based on first-principles calculation. We evaluated the feasibility of this computational approach by calculating the LTCs of 103 compounds of wurtzite, zincblende, and rocksalt types. This approach was benchmarked against our previously used conventional approach. We found that this approach significantly reduces computational demands while maintaining a satisfactory accuracy level for LTC prediction. Apart from the initial stage of generating datasets using first-principles calculations, subsequent LTC calculation steps require minimal computational resources. This enables users to calculate LTCs and various related physical values on standard computers, given access to high-quality datasets. Our future plans include the computation and

distribution of such high-quality datasets for a wide range of compounds.

TABLE III. LTC values of zincblende- and wurtzite-type compounds at 300 K in W/m-s as shown in Fig. 5 calculated through the polynomial MLPs, $z-\kappa^{\text{pMLP}}$ and $w-\kappa^{\text{pMLP}}$, respectively, and those by the conventional approach, $z-\kappa^{\text{conv}}$ and $w-\kappa^{\text{conv}}$, respectively.

	$z-\kappa^{\text{conv}}$	$z-\kappa^{\text{bMLP}}$	$w-\kappa_{xx}^{\text{conv}}$	$w-\kappa_{zz}^{\text{conv}}$	$w-\kappa_{xx}^{\text{pMLP}}$	$w-\kappa_{zz}^{\text{bMLP}}$
AgI	3.538	3.260	2.491	3.008	2.229	2.654
AlAs	79.84	79.88	68.18	66.24	62.99	61.21
AlN	232.0	233.6	269.5	243.7	271.4	244.4
AlP	79.18	79.21	71.84	65.52	71.17	65.54
AlSb	91.03	91.19	52.59	49.54	49.09	46.89
BAs	1614	1605	1535	1155	1541	1092
BeO	361.7	361.0	317.8	325.0	316.8	322.9
BeS	194.2	194.4	165.7	149.1	153.6	141.8
BeSe	447.3	443.3	345.7	333.7	342.2	327.8
BeTe	262.3	262.3	214.4	202.3	200.5	191.6
BN	1301	1290	1058	1012	1043	972.2
BP	489.5	488.3	498.5	359.9	468.0	338.1
CdS	23.67	23.52	19.81	19.99	19.40	19.71
CdSe	15.38	15.26	12.53	13.19	10.61	11.31
CdTe	8.523	8.358	6.284	7.215	6.043	6.812
CuBr	8.219	6.795	3.177	4.711	2.832	3.845
CuCl	2.056	1.681	1.452	2.483	1.383	2.224
CuH	21.44	21.16	6.248	5.724	6.202	5.949
CuI	10.68	8.844	8.773	9.872	7.777	8.821
GaAs	36.66	36.19	33.52	30.27	32.68	30.01
GaN	263.1	266.7	318.0	308.3	306.9	289.8
GaP	128.4	129.4	139.7	118.9	130.9	110.7
GaSb	37.74	37.30	28.5	21.90	25.25	20.13
InAs	25.47	25.35	24.23	23.28	22.92	22.08
InN	103.3	103.7	116.8	120.6	112.1	113.2
InP	83.65	85.97	75.73	72.38	70.61	63.27
InSb	15.21	14.96	11.76	11.84	10.96	11.08
MgTe	11.65	11.04	8.263	9.050	7.834	8.341
SiC	459.9	460.8	512.6	426.4	508.4	425.1
ZnO	64.27	63.47	51.38	59.91	50.80	57.65
ZnS	60.17	58.97	59.81	63.11	55.63	59.30
ZnSe	20.55	20.25	18.77	18.88	17.61	17.39
ZnTe	29.79	31.08	21.54	21.43	19.78	19.56

ACKNOWLEDGMENTS

This work was supported by JSPS KAKENHI Grant Numbers JP21K04632, JP22H01756, JP19H05787 and 24K08021 Some of the calculations in this study were performed on the Numerical Materials Simulator at NIMS.

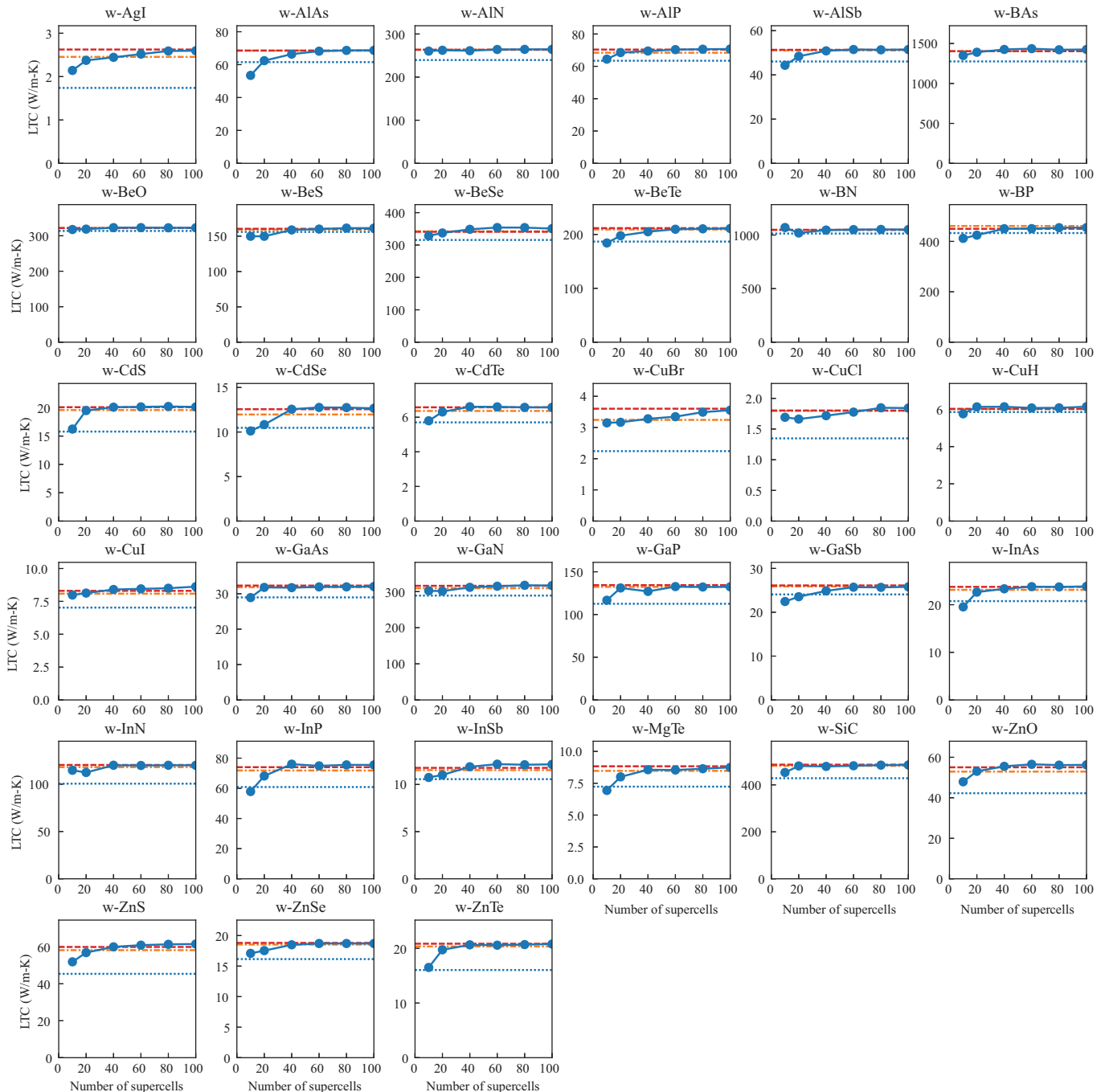


FIG. 2. Filled circles show LTCs (κ) of the 33 wurtzite-type compounds calculated at 300 K with respect to the number of supercells in the datasets used to train the polynomial MLPs. The LTC values are the averages of the diagonal elements, i.e., $(2\kappa_{xx} + \kappa_{zz})/3$. The horizontal dotted, dashed-dotted, and dashed lines depict the LTC values calculated in the conventional approach from the datasets of 100, 400, and 2000 supercells without using the polynomial MLPs, respectively.

- [1] R. E. Peierls, Zur kinetischen theorie der wärmeleitung in kristallen, *Ann. Phys.* **395**, 1055 (1929).
 [2] R. E. Peierls, *Quantum theory of solids* (Oxford University Press, 2001).

- [3] J. M. Ziman, *Electrons and phonons: the theory of transport phenomena* (Oxford University Press, 1960).
 [4] G. P. Srivastava, *Physics of phonons* (CRC Press, 1990).

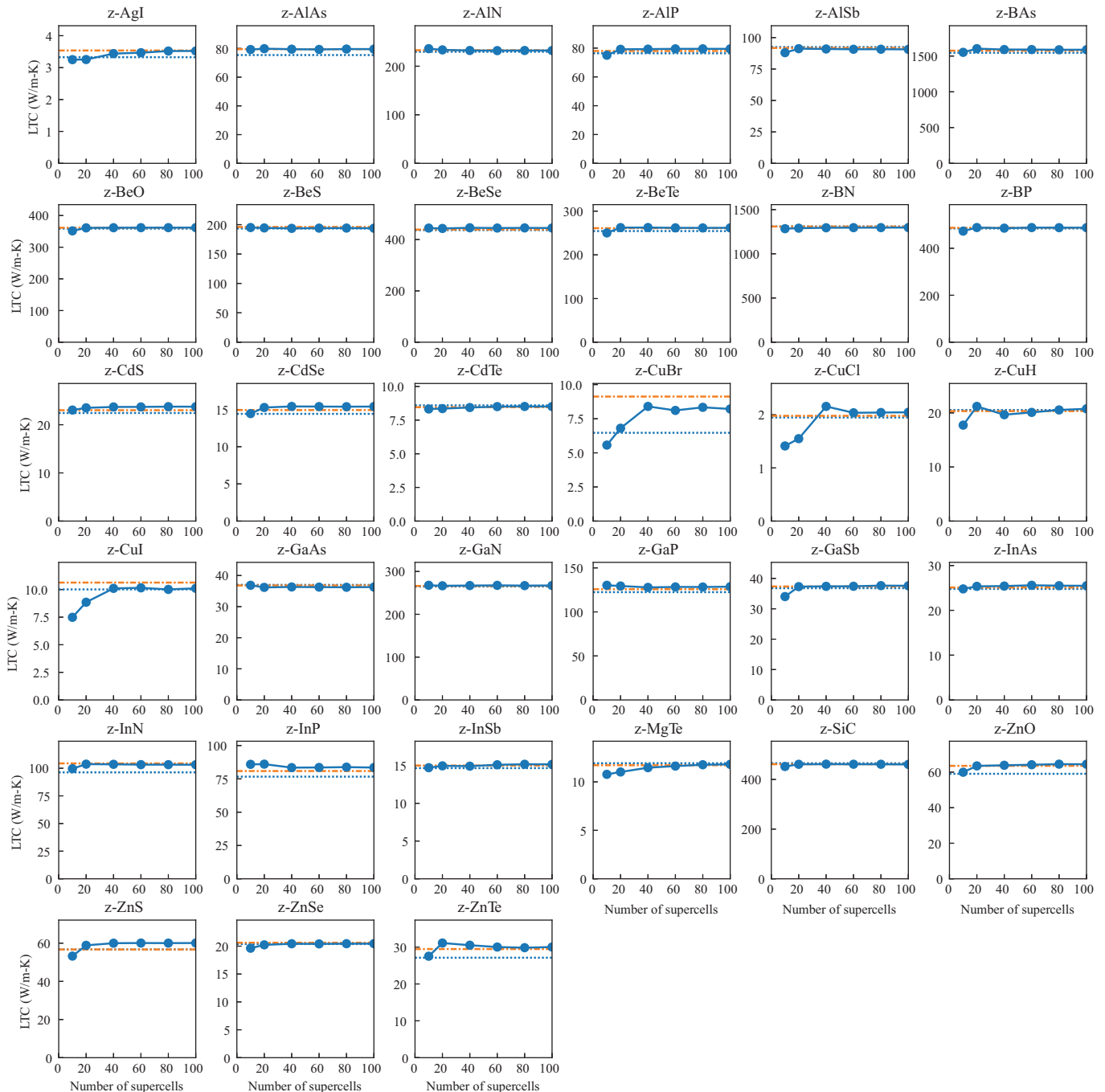


FIG. 3. Filled circles show LTCs of the 33 zincblende-type compounds calculated at 300 K with respect to the number of supercells in the datasets used to train the polynomial MLPs. The horizontal dotted and dashed-dotted lines depict the LTC values calculated in the conventional approach from the datasets of 100 and 400 supercells without using the polynomial MLPs, respectively.

- [5] T. Tadano, Y. Gohda, and S. Tsuneyuki, Anharmonic force constants extracted from first-principles molecular dynamics: applications to heat transfer simulations, *J. Phys. Condens. Matter* **26**, 225402 (2014).
- [6] J. Carrete, B. Vermeersch, A. Katre, A. van Roekeghem, T. Wang, G. K. Madsen, and N. Mingo, almabte : A solver of the space-time dependent boltzmann

- transport equation for phonons in structured materials, *Comput. Phys. Commun.* **220**, 351 (2017).
- [7] A. Chernatynskiy and S. R. Phillpot, Phonon transport simulator (phonts), *Comput. Phys. Commun.* **192**, 196 (2015).
- [8] O. Hellman, P. Steneteg, I. A. Abrikosov, and S. I. Simak, Temperature dependent effective potential

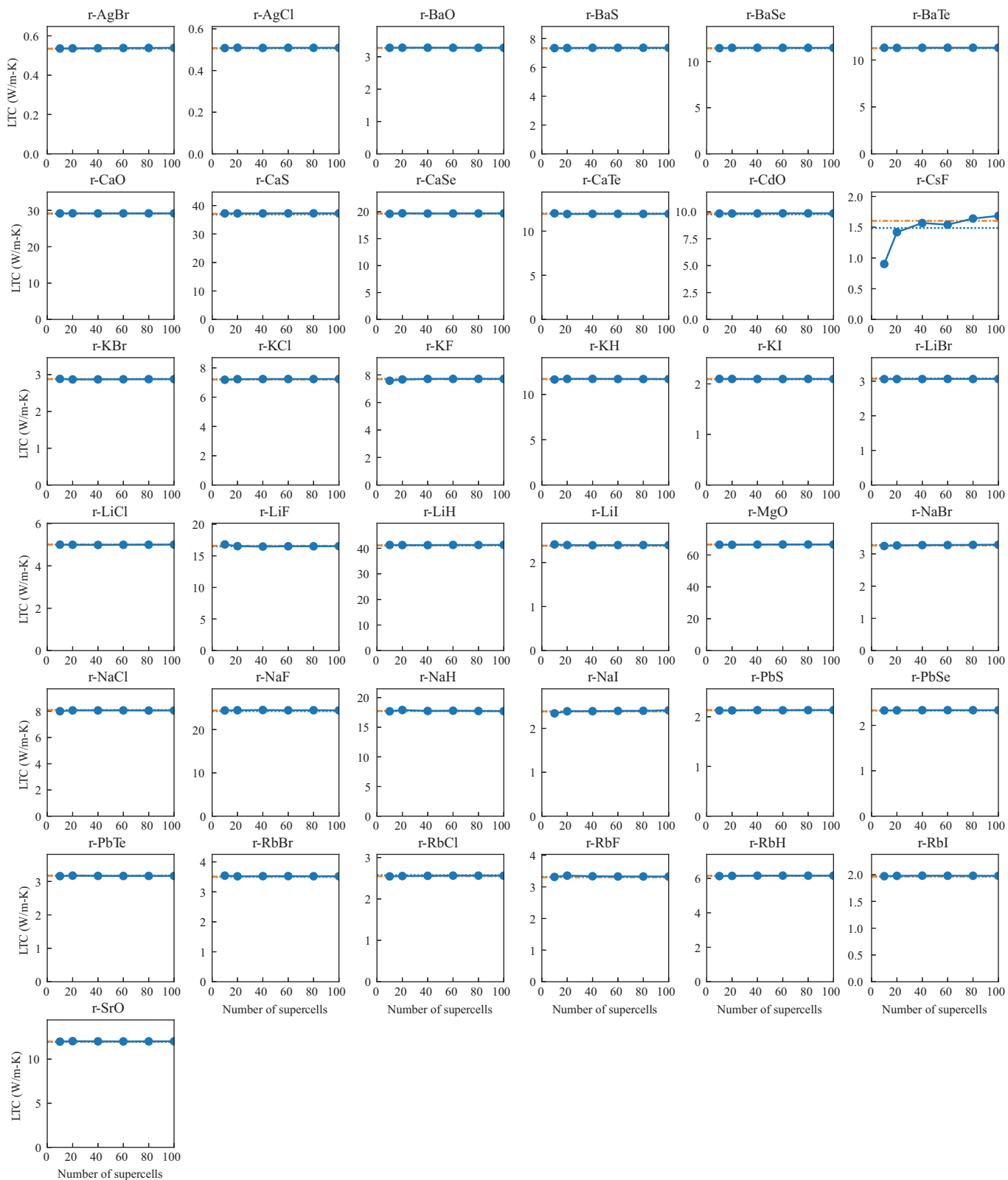


FIG. 4. Filled circles show LTCs of the 37 rocksalt-type compounds calculated at 300 K with respect to the number of supercells in the datasets used to train the polynomial MLPs. The horizontal dotted and dashed-dotted lines depict the LTC values calculated in the conventional approach from the datasets of 100 and 400 supercells without using the polynomial MLPs, respectively.

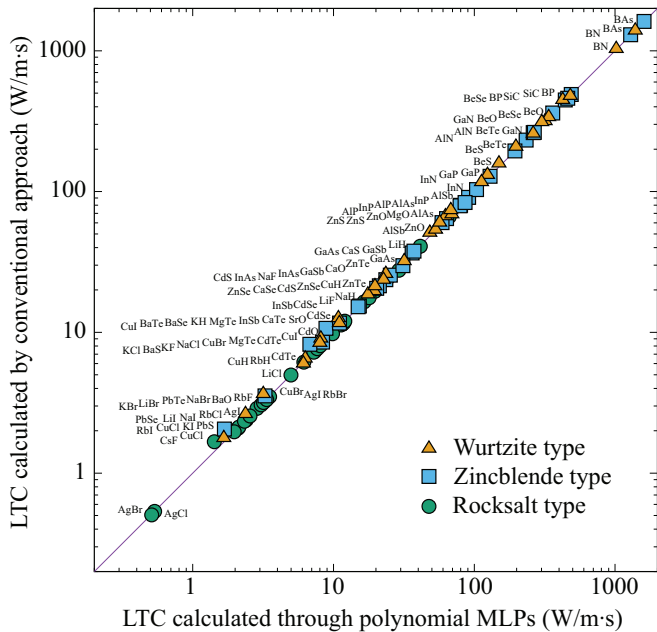


FIG. 5. Comparison between LTC values calculated through the polynomial MLPs and those by the conventional approach.[15] These values are tabulated in Tables III and IV. To train the polynomial MLPs for each compound, we employed displacement-force pairs and energies of 20 supercells obtained through first-principles calculations. For the latter LTCs, we used the finite-difference displacement-force datasets [35] from Ref. 15, comprising 1254, 222, and 146 supercells for the wurtzite-, zincblende-, and rocksalt-type compounds, respectively, to fit third-order supercell force constants.

method for accurate free energy calculations of solids, Phys. Rev. B **87**, 104111 (2013).

- [9] A. Togo, L. Chaput, and I. Tanaka, Distributions of phonon lifetimes in brillouin zones, Phys. Rev. B **91**, 094306 (2015).
- [10] W. Li, J. Carrete, N. A. Katcho, and N. Mingo, ShengBTE: a solver of the Boltzmann transport equation for phonons, Comp. Phys. Commun. **185**, 1747 (2014).
- [11] F. Zhou, W. Nielson, Y. Xia, and V. Ozoliņš, Lattice anharmonicity and thermal conductivity from compressive sensing of first-principles calculations, Phys. Rev. Lett. **113**, 185501 (2014).
- [12] T. Tadano and S. Tsuneyuki, Self-consistent phonon calculations of lattice dynamical properties in cubic SrTiO_3 with first-principles anharmonic force constants, Phys. Rev. B **92**, 054301 (2015).
- [13] A. Seko, A. Togo, and I. Tanaka, Group-theoretical high-order rotational invariants for structural representations: Application to linearized machine learning interatomic potential, Phys. Rev. B **99**, 214108 (2019).
- [14] A. Seko, Tutorial: Systematic development of polynomial machine learning potentials for elemental and alloy systems, J. Appl. Phys. **133**, 011101 (2023).
- [15] A. Togo, First-principles phonon calculations with phonoPy and phono3py, J. Phys. Soc. Jpn. **92**, 012001 (2023).

TABLE IV. LTC values of rocksalt-type compounds at 300 K in $\text{W/m}\cdot\text{s}$ shown in Fig. 5 calculated through the polynomial MLPs ($r\text{-}\kappa^{\text{PMPLP}}$) and those by the conventional approach ($r\text{-}\kappa^{\text{conv}}$).

	$r\text{-}\kappa^{\text{conv}}$	$r\text{-}\kappa^{\text{PMPLP}}$
AgBr	0.5341	0.5363
AgCl	0.5053	0.5095
BaO	3.267	3.280
BaS	7.348	7.347
BaSe	11.48	11.50
BaTe	11.28	11.30
CaO	27.52	29.18
CaS	37.10	37.23
CaSe	19.56	19.70
CaTe	11.92	11.94
CdO	9.794	9.845
CsF	1.668	1.420
KBr	2.880	2.869
KCl	7.208	7.230
KF	7.648	7.670
KH	11.58	11.72
KI	2.087	2.098
LiBr	3.057	3.058
LiCl	4.972	4.995
LiF	16.50	16.53
LiH	40.86	41.25
LiI	2.375	2.397
MgO	66.35	66.35
NaBr	3.268	3.263
NaCl	8.030	8.070
NaF	24.39	24.47
NaH	17.62	17.90
NaI	2.409	2.389
PbS	2.130	2.129
PbSe	2.331	2.331
PbTe	3.163	3.175
RbBr	3.501	3.518
RbCl	2.542	2.553
RbF	3.330	3.357
RbH	6.145	6.141
RbI	1.967	1.978
SrO	11.98	12.03

- [16] P. B. Allen and V. Perebeinos, Temperature in a peierls-boltzmann treatment of nonlocal phonon heat transport, Phys. Rev. B **98**, 085427 (2018).
- [17] A. Togo, L. Chaput, T. Tadano, and I. Tanaka, Implementation strategies in phonoPy and phono3py, J. Phys. Condens. Matter **35**, 353001 (2023).
- [18] R. M. Pick, M. H. Cohen, and R. M. Martin, Microscopic theory of force constants in the adiabatic approximation, Phys. Rev. B **1**, 910 (1970).

- [19] X. Gonze, J.-C. Charlier, D. C. Allan, and M. P. Teter, Interatomic force constants from first principles: The case of α -quartz, *Phys. Rev. B* **50**, 13035 (1994).
- [20] X. Gonze and C. Lee, Dynamical matrices, born effective charges, dielectric permittivity tensors, and interatomic force constants from density-functional perturbation theory, *Phys. Rev. B* **55**, 10355 (1997).
- [21] A. Seko and A. Togo, Symfc, <https://github.com/phonopy/symfc>.
- [22] A. Seko and A. Togo, Projector-based efficient estimation of force constants (2024), arXiv:2403.03588.
- [23] A. Togo, K. Shinohara, and I. Tanaka, Spglib: a software library for crystal symmetry search (2018), arXiv:1808.01590.
- [24] P. E. Blöchl, Projector augmented-wave method, *Phys. Rev. B* **50**, 17953 (1994).
- [25] G. Kresse, Ab-initio molecular-dynamics for liquid-metals, *J. Non-Cryst. Solids* **193**, 222 (1995).
- [26] G. Kresse and J. Furthmüller, Efficiency of ab-initio total energy calculations for metals and semiconductors using a plane-wave basis set, *Comput. Mater. Sci.* **6**, 15 (1996).
- [27] G. Kresse and D. Joubert, From ultrasoft pseudopotentials to the projector augmented-wave method, *Phys. Rev. B* **59**, 1758 (1999).
- [28] J. P. Perdew, A. Ruzsinszky, G. I. Csonka, O. A. Vydrov, G. E. Scuseria, L. A. Constantin, X. Zhou, and K. Burke, Restoring the density-gradient expansion for exchange in solids and surfaces, *Phys. Rev. Lett.* **100**, 136406 (2008).
- [29] M. Gajdoš, K. Hummer, G. Kresse, J. Furthmüller, and F. Bechstedt, Linear optical properties in the projector-augmented wave methodology, *Phys. Rev. B* **73**, 045112 (2006).
- [30] X. Wu, D. Vanderbilt, and D. R. Hamann, Systematic treatment of displacements, strains, and electric fields in density-functional perturbation theory, *Phys. Rev. B* **72**, 035105 (2005).
- [31] G. Pizzi, A. Cepellotti, R. Sabatini, N. Marzari, and B. Kozinsky, Aiiida: automated interactive infrastructure and database for computational science, *Comput. Mater. Sci.* **111**, 218 (2016).
- [32] S. P. Huber, S. Zoupanos, M. Uhrin, L. Talirz, L. Kahle, R. Häuselmann, D. Gresch, T. Müller, A. V. Yakutovich, C. W. Andersen, F. F. Ramirez, C. S. Adorf, F. Gargiulo, S. Kumbhar, E. Passaro, C. Johnston, A. Merkys, A. Cepellotti, N. Mounet, N. Marzari, B. Kozinsky, and G. Pizzi, Aiiida 1.0, a scalable computational infrastructure for automated reproducible workflows and data provenance, *Sci. Data* **7**, 300 (2020).
- [33] M. Uhrin, S. P. Huber, J. Yu, N. Marzari, and G. Pizzi, Workflows in aiiida: Engineering a high-throughput, event-based engine for robust and modular computational workflows, *Comput. Mater. Sci.* **187**, 110086 (2021).
- [34] <https://github.com/aiida-vasp/aiida-vasp>.
- [35] A. Togo, Lattice thermal conductivity calculation datasets for 103 binary compounds by finite displacement method, <https://doi.org/10.34968/nims.4370>.
- [36] L. Chaput, A. Togo, I. Tanaka, and G. Hug, Phonon-phonon interactions in transition metals, *Phys. Rev. B* **84**, 094302 (2011).